Photocatalytic decoloration of Acid Red 27 in presence of SnO_2 nanoparticles

A. Esmaielzadeh Kandjani, M. Farzalipour Tabriz, N. A. Arefian, M. R. Vaezi, F. Halek and S. K. Sadrnezhaad

ABSTRACT

In this paper, the photocatalytic decoloration of Acid Red 27 (AR27) has been investigated using ultraviolet (UV) irradiation in presence of SnO_2 nanoparticles. SnO_2 nanoparticles were synthesized via hydrothermal process. The SnO_2 nanoparticles' average crystallite sizes derived from X-ray analyses which were synthesized for 2, 12 and 24 hrs were about 3.73, 5.31 and 7.6 nm, respectively. Brunauer-Emmett-Teller (BET) analyses showed high surface area of about 183, 120 and 90(m^2/g), respectively for aforementioned synthesized samples. Our investigations indicated that reaction rate constant and photocatalytic efficiency of AR27 decoloration have a direct relation with SnO_2 nanoparticles' specific surface areas and band gap energies. Decoloration kinetics was investigated by using Langmuir–Hinshelwood model. The values of the adsorption equilibrium constant, $K_{[AR27]}$, and the kinetic rate constant of surface reaction, k_c, were found to be 0.0924 (l/mg) and 0.2535 (mg/l min), respectively.

Key words | Acid Red 27, decoloration, Nano SnO_2, photocatalyst

A. Esmaielzadeh Kandjani
M. Farzalipour Tabriz
N. A. Arefian (corresponding author)
M. R. Vaezi
F. Halek
S. K. Sadrnezhaad
Materials and Energy Research Center (MERC),
Karaj,
Iran
E-mail: *mstgahmad@gmail.com*;
meisam.fa@gmail.com;
aliarefian@yahoo.com;
vaezi9016@yahoo.com;
f-halek@merc.ac.ir;
sadrnezh@yahoo.com

INTRODUCTION

Nowadays, demand for organic dyes is expanded in several industries such as textile, paper, etc. Wastewater of these industries introduces intensive color and toxicity into aquatic environmental systems. Reactive dyes are widely used in textile industries because of simple dyeing procedure and good stability of these dyes during washing processes (O'Neill *et al.* 1999; Stolz 2001).

Adsorption of compounds on a solid phase surface constitutes the basis of most environmental processes for removing gaseous or aqueous contaminants. Using heterogeneous solid catalysts especially semiconductor photocatalysts in oxidation processes also involves the adsorption of reactant molecules on their surfaces (Safarik *et al.* 1997; Oppenländer 2003).

Photocatalytic degradation and decoloration of dyes are one of the commonly used Advanced Oxidation Processes (AOP) in wastewater treatment. These processes represent an efficient method for reducing the amounts of organic pollutants in water which entail some advantages over the mere adsorptive technologies (Herrmann *et al.* 1993; Silva *et al.* 2006). In addition, oxide semiconductor photocatalysts are known to be the most promising photocatalysts which have been used in photocatalytic decoloration of azo dyes (Daneshvar *et al.* 2007).

Optical methods are one of the vastly used approaches for electronically exciting semiconductors. When semiconductors are illuminated by a light with equal or greater energy than their band gaps, absorption of a photon can produce an electron-hole ($e^- - h^+$) charge carrier pair. In an aqueous medium the valence band (h^+_{VB}) potential is positive enough to generate hydroxyl radicals at the surface and the conduction band (e^-_{CB}) potential is negative enough to reduce molecular oxygen. Also, by decomposition of water or reaction of created holes with OH^-, reactive hydroxyl radicals can be formed. These hydroxyl radicals have high reactivity and can attack the pollutant molecules adjacent to the surface

doi: 10.2166/wst.2010.156

of photocatalysts. Also, conduction band electrons (e^-_{CB}) can form superoxide anions of oxygen which can form organic peroxides or hydrogen peroxides. These phenomena have been indicated as the primary steps of organic matter mineralization (Ramamurthy & Schanze 2003).

Various parameters affect the photocatalytic efficiency by interfering photocatalytic reactions in photocatalytic decoloration processes, e.g. band gap energy, specific surface area, degree of crystallinity and concentration of the photocatalyst, etc. (Hu *et al.* 2003; Vulliet *et al.* 2003), beside operational parameters including incident light intensity, pollutants type and concentration, etc (Kiriakidou *et al.* 1999).

SnO_2 is a wide bang gap semiconductor with the band gap of about 3.65 eV at bulk state. Nanoparticles of tin dioxide have been synthesized through different chemical routes, such as precipitation (Bose *et al.* 2002), hydrothermal (Baik *et al.* 2000; Ristic *et al.* 2002), sol-gel (Zhang & Gao 2004) and hydrolytic (Deng *et al.* 2002) methods. Among these synthesis routes hydrothermal is known as a suitable method for precise controlling growth and morphology of final particles (Byrappa & Yoshimura 2001). Nanosized SnO_2 has been used as an effective supplementary phase for various nano photocatalysts to increase their efficiency in photocatalytic processes. Despite this prominent characteristic, this material has shown low photocatalytic activity when used individually (Xia *et al.* 2008; Wang *et al.* 2009).

In present paper, SnO_2 nanoparticles with small crystallite size and high specific surface area have been synthesised and photocatalytic decoloration kinetics of these nanoparticles has been studied in detail by considering Acid Red 27 as a pollutant. Despite of the previous reports about insufficient activity of SnO_2 nanoparticles used individually as photocatalyst in waste water treatment, the obtained nanoparticles in current study indicated relatively good photocatalytic activity that can be attributed mostly to their high specific surface area.

EXPERIMENTAL

Materials

NaOH and $SnCl_4$ were purchased from Merck and used without further purification. P-25 was purchased from Degussa and used as commercial reference. AR27 was purchased from Boyakh Saz (Iran) which is a commercial dye (with purity about 96%) and used without further purification. Its chemical structure and UV absorbance spectra are shown in Figure 1.

Synthesis method

The samples were prepared via hydrothermal route. First 29.5 ml of $SnCl_4$ was added dropwisely to a 100 ml NaOH (1 M) aqueous solution. After mixing, the solution was kept in stirring until formation of a transparent solution. Then obtained solution was poured into 3 Teflon lined autoclaves (75 ml) and filled up to 80% of their volumes. Then the autoclaves were kept at 170°C for 2 (SP-1), 12 (SP-2) and 24 hours (SP-3).

The vapor pressure of pure components can be calculated from Antoine equation (Antoine 1888):

$$\log P = A - \frac{B}{C+T} \quad (1)$$

where, for water at 99–374°C, A, B and C are 8.14019, 1,810.94 and 244.485, respectively (Poling *et al.* 2000). At 170°C, the pressure which was calculated from above equation is about 7.86 bar.

After that, autoclaves were cooled to room temperature naturally and then the precipitates were filtered and washed with distilled water and ethanol for several times. Finally obtained powders dried at 50°C for 24 hours.

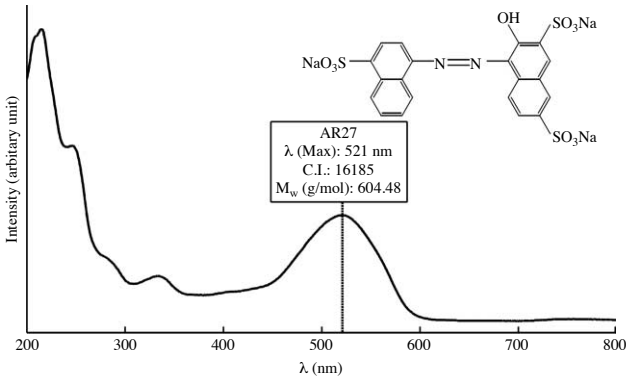

Figure 1 | The UV absorbance spectra and chemical structure of AR27.

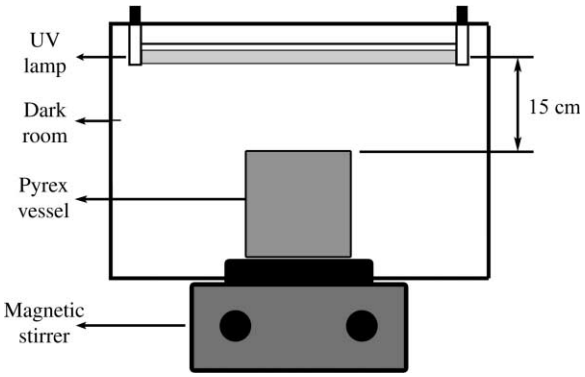

Figure 2 | Schematic diagram of the photoreactor used for experiments.

Photocatalytic procedure

All experiments were carried out in a light isolated batch photoreactor. The radiation source comprised two mercury UV lamps emitting at 254 nm (15 W, UV-C, manufactured by Philips, Holland, with 5 cm distance from each other) which were placed 15 cm above bath photoreactor (Figure 2). 20 ppm of the as prepared photocatalysts were added into 200 ml of dye solution with desired concentrations (30, 40, 60 and 80 ppm) and kept under high stirring condition at room temperature. 30 minutes was given for initial adsorption of AR27 on the surfaces of SnO_2 nanoparticles. After performing photochemical decoloration, the efficiency of process was calculated by using the following equation:

$$X = \frac{C_0 - C}{C_0} \tag{2}$$

where C_0 and C are concentrations of dye in (mg/l) before and after irradiation, respectively. The initial pHs of the all samples were adjusted to 7 by adding HCl or NH_4OH.

Analysis

X-Ray structural analysis was done by utilizing Siemens D-5000 X-ray diffractometer (XRD) with Cu-Kα radiation ($\lambda = 0.154178$ nm). Transmission Electron Microscopy (Philips CM200) was used for studying morphologies of obtained nanoparticles. AR27 concentration was analyzed with a UV–Vis spectrophotometer (Aquarius-CECIL CE9500). The specific surface areas of obtained SnO_2 nanoparticles were determined by using Brunauer-Emmet-Teller method (BET-N_2 adsorption, Micromeritics Gemini 2375).

RESULTS AND DISCUSSION

Synthesis

X-Ray diffraction patterns of obtained samples are shown in Figure 3. Brags peaks in all samples are in good agreement with rutile structure of cassiterite SnO_2 (JCPDS no.41-1445), (space group $P4_2/mnm$) and unit cell parameters of $a = 4.73727$ and $c = 3.186383$Å.

The average crystallite sizes were calculated from the full width at half maximum (FWHM) of the diffraction peaks of SnO_2 (101) planes by using the Debbye–Scherrer equation:

$$D = \frac{k\lambda}{\beta \cos\theta} \tag{3}$$

where D is the mean crystallites size; K is a grain shape dependent constant (here assumed to be 0.89 for spherical grains); λ is wavelength of the incident beam; θ is the Bragg reflection peak angle; and β is the full width at half maximum (Dinnebier & Billinge 2008). The estimated results for mean crystallites sizes of samples are listed in Table 1. It can be seen that by increasing hydrothermal synthesis time from 2 to 24 hours the mean crystallite sizes of samples increase form 3.73 to 7.6 nm.

Figure 4 shows TEM images of SP-1 sample. At first glance, at low magnification (Figure 4(a)) it can be seen that the grid is covered by thin layers of SnO_2. Also some

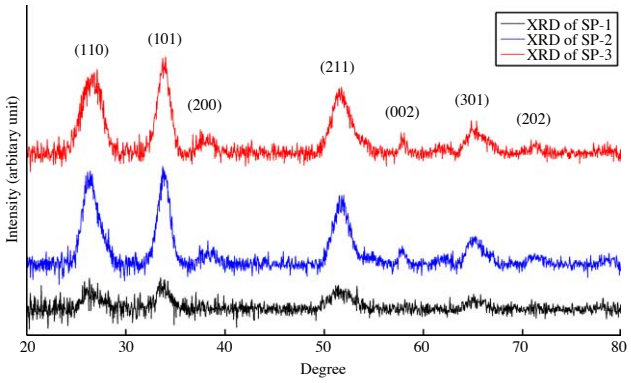

Figure 3 | XRD patterns of SP-1, SP-2 and SP-3 samples.

Table 1 | Average crystallite size, specific surface area and initial AR27 adsorption of obtained samples ($[AR27_0] = 60$ ppm and $[SnO_2] = 20$ ppm at room temperature)

Sample	Average crystallite size (from Debby–Scherrer) (nm)	Specific surface area (from BET analysis) (m^2/g)	Initial adsorption of AR27 after 30 min (calculated by using Equation (2))
SP-1	3.73 ± 0.05	183	0.071
SP-2	5.31 ± 0.05	120	0.026
SP-3	7.6 ± 0.05	90	0.008

agglomerates with median sizes of about 300 nm can be detected. But at higher magnification (Figure 4(b)) it seems that these layers and agglomerates are comprised of smaller particles with diameters of about 5 nm. Selected Area Electron Diffraction (SAED) pattern of these fine particles is shown in Figure 4(c). The four indicated diffusion rings are identified to be {211}, {310}, {312} and {411} planes sets reflections of rutile type SnO_2. Diffused rings patterns in SAED are usually attributed to extremely fine grain structures (Jiang *et al.* 2002). TEM images of SP-2 and SP-3 samples showed the same morphologies with slight increase in mean particle sizes. Due to extremely fine size and high agglomeration tendency of particles, accurate estimation of particle size distribution involves with high statistical errors. Therefore the median size of particles has not been indicated.

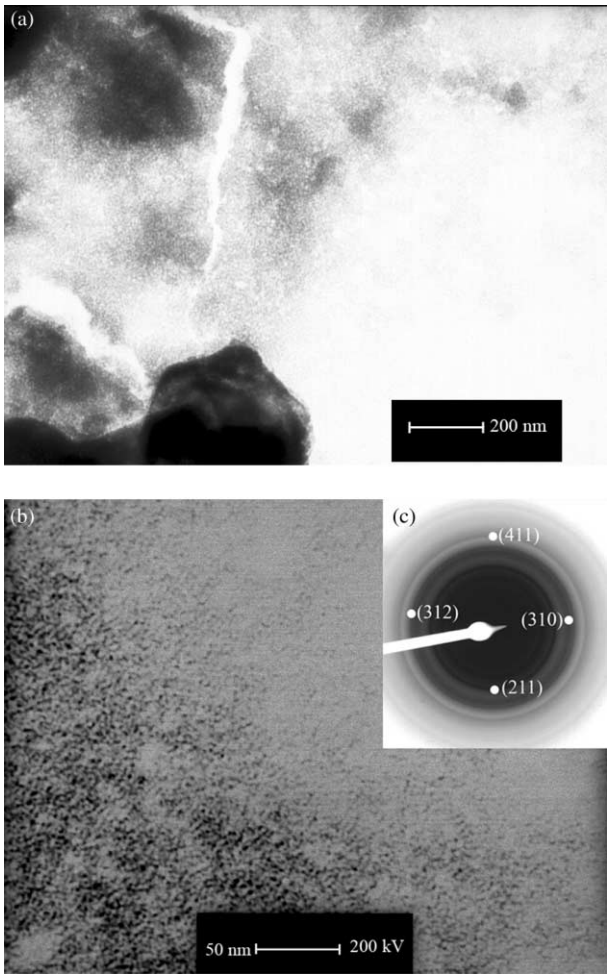

Figure 4 | TEM image of SP-1. The inset (c) is the SAED pattern of sample.

The specific surface areas of the obtained samples were calculated from Brunauer–Emmett–Teller (BET) method. These results are also listed in Table 1. The results also indicate a decrease in specific surface area by increasing hydrothermal synthesis time, which can be attributed to growth of SnO_2 particles, as mentioned before.

BET adsorption Isotherm plots of all samples, highly represents a Type I isotherm as shown in Figure 5(a). It has been shown, if a solid contains micropores, its isotherm tends to appears as a Type I isotherm. This phenomenon is due to overlap of potential fields of neighbouring porosities walls and corresponding by the increase in interaction energy of solid with gas molecules (Gregg & Sing 1982).

The Halsey equation is generally used as a statistical estimation of adsorbed film thickness as a function of nitrogen adsorption pressure at 77 K as shown in Equation (3). Using this equation is named as t-method which can be used for calculating monolayer surface areas and micropore volume sizes of powders (Halsey 1948).

$$t[\text{nm}] = 0.354\left[\frac{5}{\text{Ln}\left(\frac{P_0}{P}\right)}\right]^{(1/3)} \quad (4)$$

The results are listed in Table 2. These data which have been derived from Figure 5(b), could be used for calculating

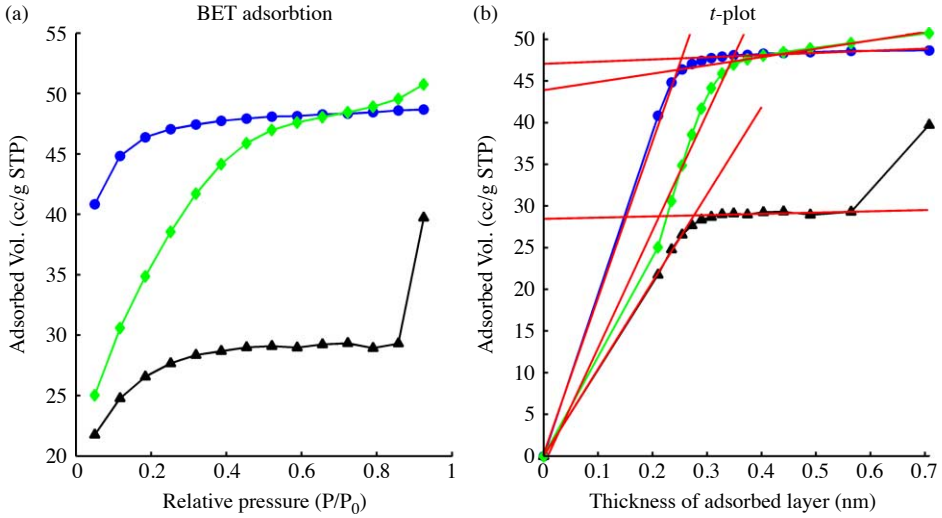

Figure 5 | a) BET adsorption isotherm and b) *t*-plot of prepared samples.

several properties as:

$$\text{Micropore volume} = 0.001547(t - \text{plot Intercept}) \quad (5)$$

$$\text{Total Area} = 1547(t - \text{plot Slope1}) \quad (6)$$

$$\text{External Area} = 1547(t - \text{plot Slope2}) \quad (7)$$

These equations could be applied only when Nitrogen gas is used as adsorbent, in other cases the constants would be different from mentioned numbers. It is assumed that pores are cylindrical, open-ended and pore networks are absent. The method involves the area of the pore walls. It uses the Kelvin equation to correlate the relative pressure of nitrogen in equilibrium with the porous solid to the size of the pores where capillary condensation takes place (Gregg & Sing 1982).

One of the most discussed mechanisms for formation of crystalline particles in hydrothermal process is based on growth unit model. In this model it is assumed that during crystallization process, cations form complexes with OH^- ions as ligands which built growth units with the same coordination number equal to the crystal. It is believed that during hydrothermal formation of SnO_2 crystals, the growth units are $Sn(OH)_6^{2-}$ complexes (Li *et al.* 1999; Wang 2008).

During the process, these units bond together by reactions between OH ligands of two adjacent units and release of water molecules as a by-product. Nuclei are formed by extension of these complexes. These nuclei grow by the same mechanism to form SnO_2 crystallites with OH^- ligands on their surfaces. After drying process the whole crystallites transform into SnO_2 crystals.

Figure 6(a) shows the optical absorption curve of SP-1 nanoparticles. The maximum UV absorbances of all samples are between 250 and 360 nm wavelengths which do not overlap with wavelengths of AR27 maximum UV absorbance (i.e. 521 nm) which was used as criteria of AR27 concentration. Decrease in nanoparticles sizes results in increase of the band gap energy (Li & Li 2006). The band gap energies of produced nanoparticles were calculated based on their optical absorbance as shown in Figure 6(b). Absorption coefficient, $\alpha(\lambda)$, for allowed direct transition of semiconductors is given by the following expression

Table 2 | Results of t-method for surface areas and micropore volume of the samples

Sample	Slope1 (cm^3 STP/g/nm)	Slope2 (cm^3 STP/g/nm)	Intercept (cm^3 STP/g)	Total area (m^2/g)	External area (m^2/g)	Micropore volume (cm^3/g)
SP-1	187.4780	2.5968	47.0607	288.9462	4.0023	0.0729
SP-2	140.6449	9.9250	43.8937	216.7658	15.2967	0.0680
SP-3	104.7074	1.5138	28.4528	161.3780	2.3330	0.0441

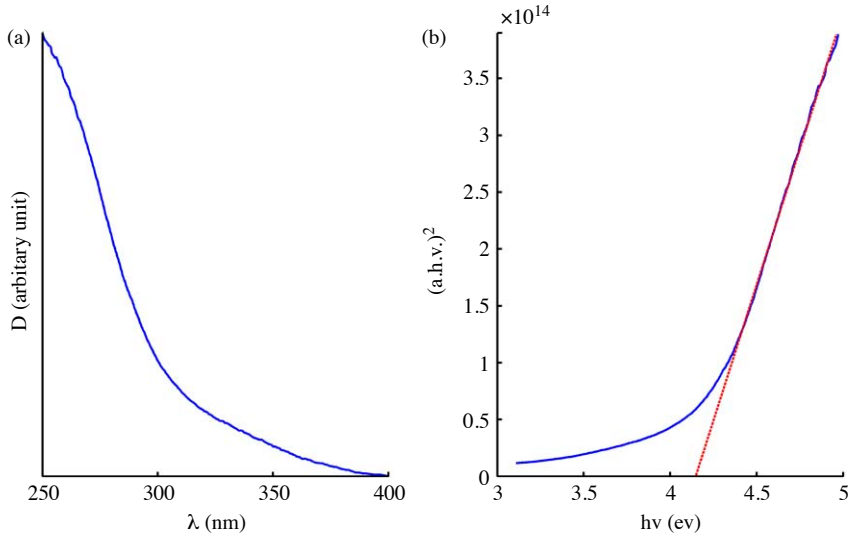

Figure 6 | a) Absorbance curve of SP-1, b) band gap of SP-1.

(Esmaielzadeh Kandjani *et al.* 2009):

$$\alpha = A\frac{(h\nu - E_g)^n}{h\nu} \tag{8}$$

where A is coefficient of the given electronic transition probability, E_g is band gap energy and is equal to 0.5 and 2 for allowed direct and indirect transitions and 1.5 and 3 in case of forbidden direct and indirect transitions, respectively. In current study the best fit of $(\alpha h\upsilon)^{1/n}$ versus photon energy was obtained 0.5. The obtained band gap energies of SP-1, SP-2 and SP-3 were 4.15, 4.02 and 3.91 eV, respectively.

Photocatalytic properties

In absence of UV irradiation, initial concentration of AR27 in presence of colloidal photocatalyst particles decreased gradually. This decrease was negligible for all samples after about 20 min which corresponds to the equilibrium adsorption of dye on the surface of photocatalysts. Thus 30 min was chosen for initial adsorption of the dye on the surface of SnO_2 nanoparticles. Also, the decoloration of AR27 under UV irradiation in absence of photocatalyst was negligible. Figure 7 Shows the UV–Vis absorbance spectra of dissolved AR27 (60 ppm) in water with SP-1 colloidal nanoparticles (20 ppm). These spectra indicate the dependence of AR27 UV–Vis absorbance intensity on irradiation time. The amounts of these initial adsorptions are listed in Table 1. This step is essential for adsorption of dye on the surface of photocatalysts and accurate estimation of photocatalytic efficiency.

According to Figure 7, the changes in the dye concentration during the photocatalytic decoloration with different nanoparticles are shown in Figure 8. As it can be seen in this figure, the photocatalytic efficiencies of obtained SnO_2 nanoparticles, due to their high specific surface areas, are much higher than commercial P-25 nano TiO_2 photocatalyst.

The total active surface area decreases by increase in photocatalyst's mean particles size. This causes the total amount of adsorbed AR27 on the surface of SnO_2 nanoparticles to decrease. These amounts are listed in Table 1.

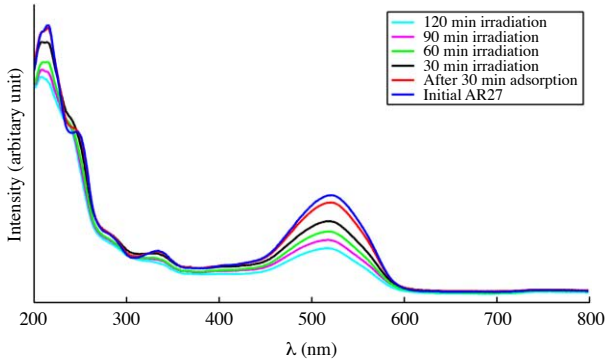

Figure 7 | Variations of UV–Vis absorbance spectra for $[AR27]_0 = 60$ ppm in aqueous SnO_2 colloids solutions $[SnO_2]_{SP\text{-}1} = 20$ ppm after different irradiation times.

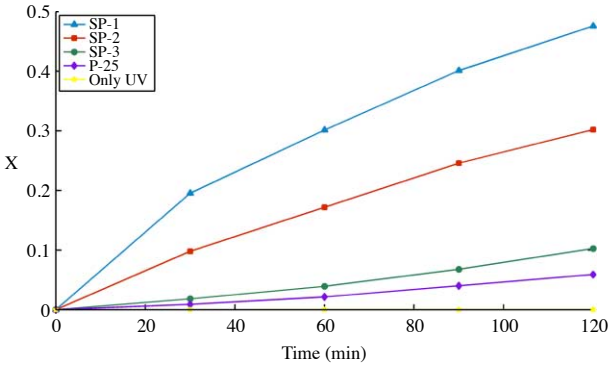

Figure 8 | Variations of decoloration efficiency (X) vs. time with $[AR27]_0 = 60$ and [photocatalyst] = 20 ppm.

Also, the decrease in active surface sites of the semiconductors due to particles growth alters the amount of electron-hole trapping on the surface of nanoparticles and thus decreases the photo-induced processes (Al-Ekabi & Serpone 1998).

Kinetics of AR27 photocatalytic decoloration

Most of the organic azo dyes decoloration reactions by photocatalysts and UV light are pseudo-first-order. By assuming pseudo-first-order photocatalytic decoloration reaction of AR27, its concentration in any given time can be estimated as following:

$$-\mathrm{Ln}\left(\frac{[\mathrm{AR27}]}{[\mathrm{AR27}]_0}\right) = k_{obs} \cdot t \qquad (9)$$

Where, k_{obs} is the pseudo-first-order rate constant.

Figure 9 shows the variation of $-\mathrm{Ln}([AR27]/[AR27]_0)$ versus irradiation time for the AR27 solutions treated by SP-1, SP-2 and SP-3 nanophotocalalysts. The values of k_{obs} which were obtained from the slopes of least square fits of $-\mathrm{Ln}([AR27]/[AR27]_0)$ data vs. Time are 0.0056, 0.003 and 0.0008 (1/min) for SP-1, SP-2 and SP-3 samples, respectively. As expected for SP-1 sample, which had the largest specific surface area, the amount of its k_{obs} for AR27 decoloration was higher than the others, while decolouration by SP-3 had the lowest rate constant in comparison with SP-1 and SP-2.

If same procedure was carried out with different initial concentrations of AR27, due to changing the concentration of active organic azo dyes molecules adjacent to photocatalysts surface and constant rate of electron-hole creation on the surface of photocatalysts, the k_{obs} would have changed (Mills *et al.* 1993). Figure 10 shows a plot of $-\mathrm{Ln}([AR27]/[AR27]_0)$ versus irradiation time for SP-1 with different initial concentrations of AR27. Again, the values of k_{obs} were obtained from least square fit. The obtained results show that by increasing the initial concentration of AR27 from 30 to 80 ppm, k_{obs} values decrease from 0.0198 to 0.0031 (1/min). The values of k_{obs} for all experiments are listed in Table 3.

The pseudo-first order of azo dyes decoloration reaction with UV/Photocatalysts can be related to the surface adsorp tion of dyes on the active sites without saturation (Peill & Hoffmann 1998). By assuming Langmuir–Hinshelwood kinetic model (Luo & Ouis 1996), AR27 decoloration reaction rate would be proportional to the surface coverage of photocatalytic particles with

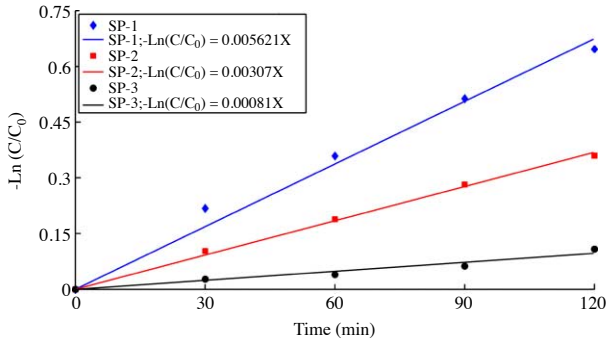

Figure 9 | Determination of the pseudo-first-order kinetic rate constant, k_{obs}, for [photocatalyst] = 20 ppm and $[AR27]_0 = 60$ ppm.

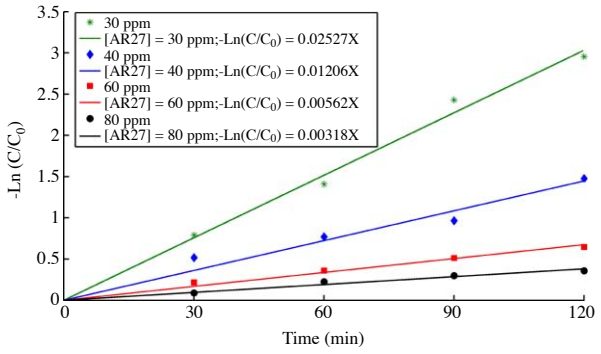

Figure 10 | Variations of decoloration rate constant vs. AR27 initial concentration in presence of $[SnO_2]_{SP\text{-}1} = 20$ ppm.

Table 3 | AR27 decoloration efficiency after 60 min and k_{obs} constants of photocatalytic reactions in different conditions

Sample	$[photocatalyst]_0$ (ppm)	$[AR27]_0$ (ppm)	X (60 min)	k_{obs}(1/min)	k_{obs}^{-1} (min)
SP-1	20	30	0.773	0.02527	50.5051
SP-1	20	40	0.537	0.01206	88.4956
SP-1	20	60	0.301	0.00562	188.6792
SP-1	20	80	0.202	0.00318	322.5806
SP-2	20	60	0.172	0.00307	333.3333
SP-3	20	60	0.019	0.00081	1,250

organic substance,

$$k_c \frac{K_{AR27}}{1 + K_{AR27}[AR27]_0} = k_{obs} \quad (10)$$

$$\frac{1}{k_{obs}} = \frac{1}{k_c K_{AR27}} + \frac{[AR27]_0}{k_c} \quad (11)$$

where K_{AR27} is the adsorption equilibrium constant, k_c is the surface reaction rate constant and $[AR27]_0$ is the initial concentration of AR27.

In the Langmuir–Hinshelwood equation k_c is related to the limiting rate of the reaction at maximum coverage under the experimental conditions and K_{AR27} represents the equilibrium constant for adsorption of AR27 on the active surface sites of photocatalysts (Turchi & Ollis 1990). As shown in Figure 11 by least square fitting, the values of the adsorption equilibrium constant, K_{AR27} and the rate constant of surface reaction, k_c were calculated to be 0.0924 (l/mg) and 0.02535 (mg/min l), respectively.

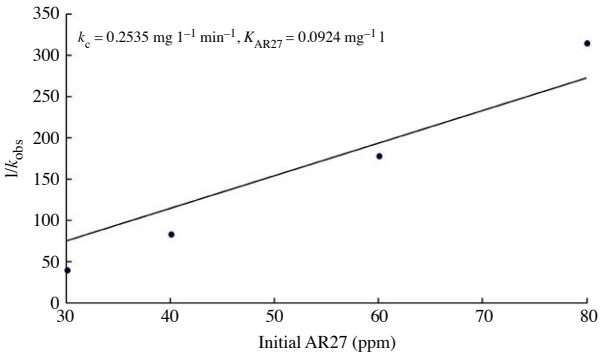

Figure 11 | Langmuir–Hinshelwood plot of ($1/k_{obs}$) vs. Initial concentration of AR27 and its least square fit for $[SnO_2]_{SP\text{-}1} = 20$ ppm.

CONCLUSION

In this paper, synthesis of SnO_2 nanoparticles with high specific surface area of 183 m^2/g and small mean crystallite size of 3.73 nm were reported and their photocatalytic activity and decoloration reaction kinetics were discussed in terms of Langmuir–Hinshelwood kinetic model. The synthesized nanoparticles showed Type-I adsorption isotherm which was attributed to microporous structure. The samples pores volumes decreased from 0.0729 to 0.0441 cm^3/g and their specific surface areas decreased from 183 to 90 m^2/g with increasing hydrothermal synthesis time from 2 to 24 hours, also the corresponding band gap energies decreased from 4.15 to 3.91 eV, respectively. Increase in specific surface areas and band gap energies of the samples caused an increase in decoloration observed reaction rate constants (k_{obs}) of AR27 from 0.0008 to 0.0056. Thus due to their high specific surface area and also high decoloration efficiency, the obtained nanoparticles can be used as promising contaminants adsorbent and good photocatalysts for decoloration of low concentrations of the investigated dye.

REFERENCES

Al-Ekabi, H. & Serpone, N. 1998 Kinetic studies in heterogeneous photocatalysis. 1. Photocatalytic degradation of chlorinated phenols in aerated aqueous solutions over TiO_2 supported on a glass matrix. *J. Phys. Chem.* **92**, 5726–5731.

Antoine, C. 1888 Tensions des vapeurs: nouvelle relation entre les tensions et les temperatures (vapour pressures: new relation between the pressure and the temperature). *Comptes Rendus des Séances de l'Académie des Sciences* **107**, 681–684.

Baik, N. S., Sakai, G., Miura, N. & Jamazoe, N. 2000 Preparation of stabilized nanosized tin oxide particles by hydrothermal treatment. *J. Am. Ceram. Soc.* **83**, 2983–2987.

Bose, A. C., Kalpana, D., Thangadurai, P. & Ramasamy, S. 2002 Synthesis and characterization of nanocrystalline SnO_2 and fabrication of lithium cell using nano-SnO_2. *J. Power Sources* **107**, 138–141.

Byrappa, K. & Yoshimura, M. 2001 *Handbook of Hydrothermal Technology: A Technology for Crystal Growth and Materials Processing*. Noyes Publications, USA, pp. 27–32.

Daneshvar, N., Aber, S., Seyed Dorraji, M. S., Khataee, A. R. & Rasoulifard, M. H. 2007 Photocatalytic degradation of the insecticide diazinon in the presence of prepared

nanocrystalline ZnO powders under irradiation of UV-C light. *Sep. Purif. Technol.* **58**, 91–98.

Deng, Z. X., Wang, C. & Li, Y. D. 2002 New hydrolytic process for producing zirconium dioxide, tin dioxide, and titanium dioxide nanoparticles. *J. Am. Ceram. Soc.* **85**, 2837–2839.

Dinnebier, R. E. & Billinge, S. J. L. 2008 *Powder Diffraction Theory and Practice*, 1st edition. The Royal Society of Chemistry, UK, pp. 142–146.

Esmaielzadeh Kandjani, A., Shokuhfar, A., Farzalipour Tabriz, M., Arefian, N. A. & Vaezi, M. R. 2009 Optical properties of Sol-Gel prepared nano ZnO: the effects of aging period and synthesis temperature. *J. Optoelectron. Adv. Mater.* **11**, 289–295.

Gregg, S. J. & Sing, K. S. W. 1982 *Adsorption, Surface Area and Porosity*, 2nd edition. Academic Press, London, pp. 195–209.

Halsey, G. 1948 Physical adsorption on non-uniform surfaces. *J. Chem. Phys.* **16**, 931–937.

Herrmann, J. M., Guillard, C. & Pichat, P. 1993 Heterogeneous photocatalysis: an emerging technology for water treatment. *Catal. Today* **17**, 7–20.

Hu, C., Yu, J. C., Hao, Z. & Wong, P. K. 2003 Effects of acidity and inorganic ions on the photocatalytic degradation of different azo dyes. *Appl. Catal. B: Environ.* **46**, 35–47.

Jiang, J. C., Lian, K. & Meletis, E. I. 2002 Influence of oxygen plasma treatment on the microstructure of SnO_x thin films. *Thin Solid Films* **411**, 203–210.

Kiriakidou, F., Kondarides, D. I. & Verykios, X. E. 1999 The effect of operational parameters and TiO_2-doping on the photocatalytic degradation of azo-dyes. *Catal. Today* **54**, 119–130.

Li, M. & Li, J. C. 2006 Size effect on the band gap of semiconductor compounds. *Mater. Lett.* **60**, 2526–2529.

Li, W. J., Shi, E. W., Zhong, W. Z. & Yin, Z. W. 1999 Growth mechanism and growth habit of oxide crystals. *J. Cryst. Growth* **203**, 186–196.

Luo, Y. & Ouis, D. 1996 Heterogeneous photocatalytic oxidation of trichloroethylene and toluene mixtures in air: kinetic promotion and inhibition, time-dependent catalyst activity. *J. Catal.* **163**, 1–11.

Mills, A., Davis, R. H. & Worsely, D. 1993 Water purification by semiconductor photocatalysis. *Chem. Soc. Rev.* **22**, 417.

O'Neill, C., Hawkes, F. R., Hawkes, D. L., Lourenco, N. D., Pinheiro, H. M. & Delee, W. 1999 Colour in textile effluents: sources, measurement, discharge consents and simulation: a review. *J. Chem. Technol. Biotechnol.* **74**, 1009–1018.

Oppenländer, T. 2003 *Photochemical Purification of Water and Air*, 1st edition. WILEY-VCH Verlag Gmbh & Co. KGaA, Weinheim, Germany, pp. 123–124.

Peill, N. J. & Hoffmann, M. R. 1998 Mathematical model of photocatalytic fiber-optic cable reactor for heterogeneous photocatalysis. *Environ. Sci. Technol.* **32**, 398–404.

Poling, B. E., Prausnitz, J. M. & O'Connell, J. P. 2000 *The Properties of Gas and Liquids*, 5th edition. McGraw-Hill, New York, p. 669.

Ramamurthy, V. & Schanze, K. S. 2003 *Semiconductor Photochemistry And Photophysics*. Marcel Dekker Inc, USA, pp. 236–238.

Ristic, M., Ivanda, M., Popovic, S. & Music, S. 2002 Dependence of nanocrystalline SnO_2 particle size on synthesis route. *J. Non-Cryst. Solids* **303**, 270–280.

Safarik, I., Nymburska, K. & Safaikova, M. 1997 Adsorption of water-soluble organic dyes on magnetic charcoal. *J. Chem. Technol. Biotechnol.* **69**, 1–4.

Silva, C. G., Wang, W. & Faria, J. L. 2006 Photocatalytic and photochemical degradation of mono-, di- and tri-azo dyes in aqueous solution under UV irradiation. *J. Photochem. Photobiol. A* **181**, 314–324.

Stolz, A. 2001 Basic and applied aspects in the microbial degradation of azo dyes. *Appl. Microbiol. Biotechnol.* **56**, 69–80.

Turchi, C. S. & Ollis, D. F. 1990 Photocatalytic degradation of organic contaminants: mechanisms involving hydroxyl attack. *J. Catal.* **122**, 178–192.

Vulliet, E., Chovelon, J. M., Guillard, C. & Herrmann, J. M. 2003 Factors influencing the photocatalytic degradation of sulfonylurea herbicides by TiO_2 aqueous suspension. *J. Photochem. Photobiol. A* **159**, 71–79.

Wang, W. W. 2008 SnO_2/α-Fe_2O_3 hierarchical nanostructure: hydrothermal preparation and formation mechanism. *Mater. Res. Bull.* **43**, 2055–2059.

Wang, H., Baek, S., Lee, J. & Lim, S. 2009 High photocatalytic activity of silver-loaded ZnO-SnO_2 coupled catalysts. *Chem. Eng. J.* **146**, 355–361.

Xia, H., Zhuang, H., Zhang, T. & Xiao, D. 2008 Visible-light-activated nanocomposite photocatalyst of Fe_2O_3/SnO_2. *Mater. Lett.* **62**, 1126–1128.

Zhang, J. & Gao, L. 2004 Synthesis and characterization of nanocrystalline tin oxide by sol-gel method. *J. Solid State Chem.* **177**, 1425–1430.